Structural, photocatalytic and surface analysis of Nb/Ag codoped TiO$_2$ mesoporous nanoparticles

Mahtab Gorgani[1] · Behzad Koozegar Kaleji [1]

Abstract

In this study, several TiO$_2$ mesoporous nanoparticles with different mol% of niobium and silver were synthesized using the sol–gel method. The crystalline phase, chemical state, photocatalytic and optical properties, specific surface area, and morphology of mesoporous nanoparticles were characterized by X-ray diffraction (XRD), X-ray photoelectron spectroscopy (XPS), UV–Vis reflective spectroscopy (UV–Vis), Brunauer–Emmett–Teller-specific surface area (BET) and field emission scanning electron microscopy (FESEM). With increasing calcination temperature, the photocatalytic activity of the samples gradually increased due to the improvement of crystallization of the anatase and rutile phases. Nb/Ag codoping sample calcined at 550 °C has reduced the band gap energy (3.17 eV to 3.06 eV) and improved the photocatalytic properties of samples under visible light (xenon lamp, 200 W for 1 h and 2 h). Doped TiO$_2$ mesoporous nanoparticles were shown to have the highest photocatalytic activity as compared with the pure TiO$_2$ nanoparticles. The best photocatalytic efficiency of codoped TiO$_2$ mesoporous nanoparticles was observed for the TNA3 sample calcined under 550 °C, containing molar contents of Nb (0.5 mol%) and Ag (1 mol%) dopant ions with 95.60% efficiency.

Graphical Abstract

Synthesis of Nb/Ag-codoped TiO$_2$ (TNA) nanoparticles by sol–gel method
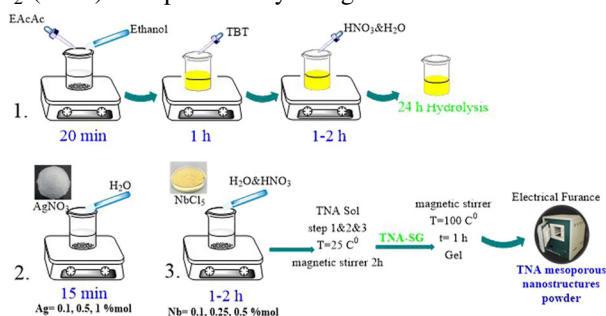
Keywords Mesoporous nanoparticles · Nb/Ag-codoped TiO$_2$ · Sol–gel synthesis · Photocatalytic properties

✉ Behzad Koozegar Kaleji
  bkaleji@yahoo.com

1 Department of Materials Engineering, Faculty of Engineering,
   Malayer University, P.O. Box 65719-95863, Malayer, Iran

Highlights

- Nb/Ag additive enhanced significantly photocatalytic properties of TiO_2 based nanoparticles for remove of organic compounds (MB).
- Structural, optical and surface analysis of samples dependent to dopant concentration.
- Nb/Ag codoped TiO_2 nanoparticles is promising for photocatalytic properties in visible light.

1 Introduction

Nanostructured materials are widely used in various fields because of their unique properties. Nowadays, nanostructured titania has received much attention due to its high potential in photocatalytic applications, self-cleaning coatings, photovoltaic, heavy metal removal from industrial effluents, ceramic membranes, and gas sensors [1]. Among nanostructured materials, TiO_2 as a semiconductor is very useful in these applications. However, because of the wide band gap (3.2 eV), it only has photocatalytic activity under ultraviolet (UV) light at wavelengths <387.5 nm. Since sunlight comprises about 45% of visible light and 5% of UV light, so much research has been done to reduce the band gap in this semiconductor [2]. Titania's photocatalytic activity depends on several factors, such as particle size, crystalline phase, band gap, specific surface area, and pore volume [3]. The rate of photocatalytic decomposition of titania nanoparticles is limited by the rate of electron–hole recombination. To reduce the electron–hole pair recombination, doping of intermediates or alkali metals and semiconductor coupling is commonly used [4, 5].

Much research, such as metal, non-metallic dopant, titania semiconductor coupling with other oxide semiconductors with a narrow band gap, codoping with different cations and anions, has been done to improve TiO_2 photocatalytic efficiency under visible light [6, 7]. One of the effective methods for reducing the band gap of TiO_2 semiconductor is the presence of Ti^{3+} and oxygen vacancy that is usually done by adding dopants to the titania structure, which results in improved titania photocatalytic activity in the visible light region [8–11]. The effect of dopant content and calcination temperature on the activity of Ag/Cu-codoped TiO_2 catalysts was investigated [12]. The stability of the anatase phase was increased with codoping of silver and copper to TiO_2 lattice. Khatun et al. [13] investigated the codoping effect of Ga and V on the optical and crystalline properties of titania. The results of this study showed that in the presence of codoping, the anatase phase was stable and the band gap of the sample decreased and the photocatalytic properties improved under visible light irradiation. Chena et al. [14] investigated the codoping effects of silver and nitrogen (with different percentages) on the photocatalytic properties of titania nanostructures. The nanoparticles were synthesized by the sol–gel method. Doped titania nanoparticles with 2% N and 5% Ag calcined at 400 °C had better photocatalytic properties than other samples.

According to previous research that has been done in this field, no research has been done on the synthesis of niobium/silver-codoped mesoporous titania nanoparticles by sol–gel method. Therefore, a series of Nb/Ag-codoped TiO_2 nanoparticles were prepared with different amounts of Nb and Ag (samples code: TNA1: 0.1%Nb-0.1%Ag, TNA2: 0.25%Nb-0.5%Ag, TNA3: 0.5%Nb-1%Ag, TNA4: 0.1% Nb-1%Ag). Then, the effect of codoping of niobium/silver with different mole percentages on the structural, optical, photocatalytic, and surface properties of titania mesoporous nanoparticles was investigated. Also, the efficiency of these samples as photocatalysts for the photodegradation of MB, under visible light, was investigated.

2 Experimental procedures

2.1 Materials

Titanium (IV) butoxide (TBT = $Ti(OC_4H_9)_4$), Ethanol (EtOH = C_2H_5OH), Ethyl acetoacetate (EAcAc), Nitric acid (HNO_3), Niobium chloride ($NbCl_5$), and Silver nitrate ($AgNO_3$). Methylene blue (MB) were used as a model compound in the photocatalytic activity measurements. TBT and MB was purchased from Sigma-Aldrich. Other compounds were obtained from Merck Company. All the chemicals utilized in this work were analytical grade.

2.2 Experimental procedure

In this study, Nb/Ag-codoped TiO_2 mesoporous nanoparticles were synthesized by the sol–gel method (Fig. 1). Briefly, 20 ml of ethanol and 2.55 ml of ethyl acetoacetate (EAcAc is as a sol stabilizer) were mixed, and then 3.45 ml TBT was added to the mixture at the ambient temperature (step 1). The solution was continuously stirred for 60 min, followed by the dropping of HNO_3 (0.45 ml), a catalyst to the solution until a pH of 5. De-ionized water (1.8 ml) was added to the solution slowly to initiate the hydrolysis process (stirring about 60–90 min). Yellow transparent solution (step 1: TiO_2 sol) was aged for 24 h to complete all reactions. According to Table 1, two solutions of niobium and silver (step 2 and 3) added with appropriate mole% (Table 1: Nb = 0.1, 0.25, 0.5 mole%, Ag = 0.1, 0.5, 1 mole%) to the TiO_2 sol. Then stir the prepared solution on the magnetic stirrer for 1 h and heat to the gel. Finally, the dried gel

Fig. 1 A schematic to represent the sol–gel process for synthesis of Nb/Ag-codoped TiO$_2$ (TNA) nanoparticles
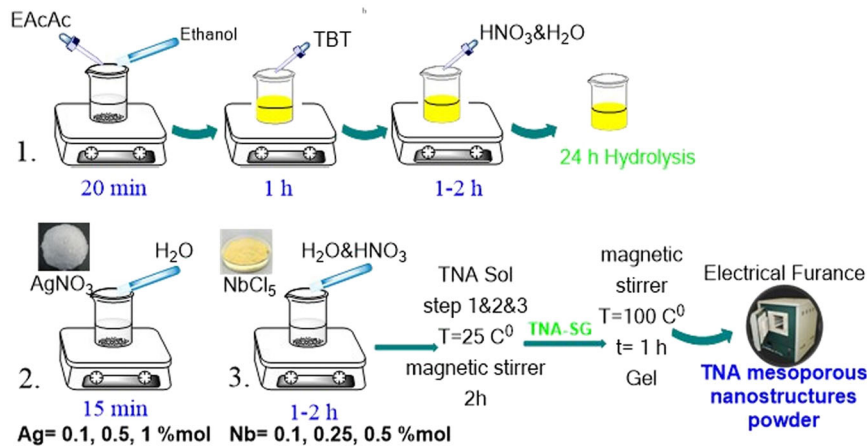
Table 1 Sample codes and dopant mole percentage. (T: TiO$_2$, N: Nb, A: Ag)

Sample code	Nb (mole%)	Ag (mole%)
TNA1	0.1	0.1
TNA2	0.25	0.5
TNA3	0.5	1
TNA4	0.1	1

was placed in the furnace and calcined at different temperatures to synthesize the desired nanoparticles. The different steps of nanoparticle preparation are shown in Fig. 1.

2.3 Nanoparticle characterization methods

Differential thermal analysis (DTA) and thermogravimetric (TG) were used to determine the crystallization temperature in the air with a heating rate of 10 °C/min (P1-STA 1640 equipment). XRD pattern and phase identification of nanopowders were recorded using X-ray diffraction analysis (Philips, MPD-XPERT, λ: Cu$_{k\alpha}$ = 0.154 nm). The samples were scanned in the 2θ range of 20–80°. The specific surface area of the nanoparticles was measured by Nitrogen gas using the Brunner–Emmett–Teller (BET) isothermal adsorption method and the pore size distribution was studied by the BJH model at different temperatures using Belsorp mini Japan. N$_2$ adsorption–desorption isotherms were determined in a surface analyzer equipment at 77 K. Spekol-2000 spectrophotometer from Germany was used to measure the optical properties for measuring the band gap and photocatalytic degradation of nanoparticles. X-ray photoelectron spectroscopy (XPS) spectra were recorded by a PHI 5000C ESCA spectrometer using Mg K_α radiation ($h\upsilon$ = 1253.6 eV). The pressure of the analyzer chamber was maintained at 5×10^{-8} Pa. Spectra were calibrated concerning, for, to the C1s peak at 284.6 eV.

Morphology of the mesoporous nanopowders was observed using field emission scanning electron microscopy (FESEM, MIRA3-TESCAN) with an accelerating voltage of 10–15 kV.

2.4 Photocatalytic activity and optical band gap

The photocatalytic degradation of organic pollutants by the samples was evaluated by the degradation of MB as a model pollutant solution under visible light irradiation by xenon lamp (200 W). The photocatalytic experiment was carried out by taking 0.2 g of each sample in 20 ml MB solutions (10 ppm). Before visible light irradiation, these solutions were stirred magnetically for 30 min in the dark place to achieve the adsorption–desorption equilibrium. The above solutions were irradiated with visible light and after every 20 min, a 3 ml sample of the solution was taken, from which the catalyst was separated by centrifugation to obtain a clear liquid. The photodegradation rates of the MB solution at given intervals of irradiation was analyzed using a UV–Vis spectrophotometer. The degradation percentage of MB, which represents the photocatalytic efficiency of the samples, can be determined by Eq. 1.
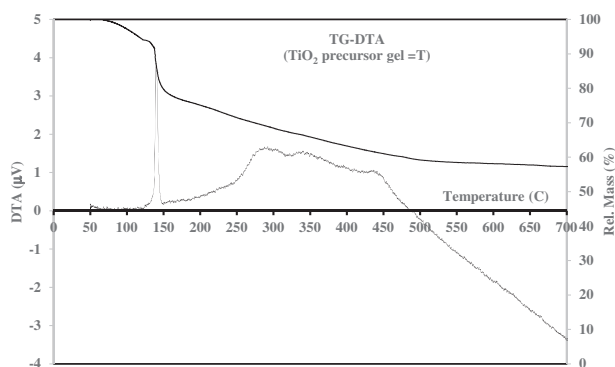
$$\eta = \left(1 - \frac{A_t}{A_0}\right) \times 100 \tag{1}$$

where η is photocatalytic efficiency of MB, A_t is absorption after radiation and A_0 is absorption before radiation [15].

The amount of rutile in the samples was calculated using the equation [16]:

$$X_R = \left(1 + \frac{0.8I_A}{I_R}\right)^{-1} \tag{2}$$

where X_R is the mass fraction of rutile in the samples, and I_A and I_R are the X-ray integrated intensities of (101) reflection of the anatase and (110) reflection of rutile, respectively.

Fig. 2 TG and DTA curves of precursor gel (T)

Fig. 3 XRD patterns of undoped (T) and Nb/Ag-codoped TiO$_2$ mesoporous nanoparticles (TNA) calcined at 350 °C for 1 h

The optical band gap corresponds to the absorption limit and can be roughly evaluated by using following equation:

$$E_g = \frac{1240}{\lambda_{\text{edge}}} (\text{eV}) \tag{3}$$

where λ_{edge} represents the absorption limit of the semiconductor. λ_{edge} can be extracted from the absorption spectrum by carrying out the first derivative of absorbance with respect to wavelength near the absorption edge and finding the point at which the derivative spectrum reaches its minimum value. This point is actually the reflection point of the absorption curve. The tangent line of the absorption curve at the reflection point intersects with the x-axis on which absorbance reaches 0 and indicates λ_{edge}.

3 Results and discussion

3.1 TG-DTA analysis

One of the effective factors in the photocatalytic behavior of titania is the formation of anatase crystalline phase or rutile resulting from the appropriate calcination temperature, so it is necessary to determine this temperature. Figure 2 shows the differential thermal analysis curves (TG-DTA) of the titania precursor gel. Thermal analysis was carried out from 50 °C to 700 °C with a heating rate of 10 °C/min in an air atmosphere. According to the TG curve, the weight loss of the sample gradually increased with increasing temperature up to about 600 °C but above this temperature, with the increase in temperature, there were very minor changes in weight loss (total weight loss during this process for T sample equals 42%). Weight loss occurs in three stages. The first stage is in the temperature range of 0–120 °C. Weight loss is about 6.2% due to the evaporation of solvent and water, which is physically absorbed. The second stage of weight loss occurs in the temperature range of 120–150 °C, which is about 16.8%. This weight loss is related to the removal of residual organic matter and residual water. Third, weight loss occurs at about 19% in the temperature
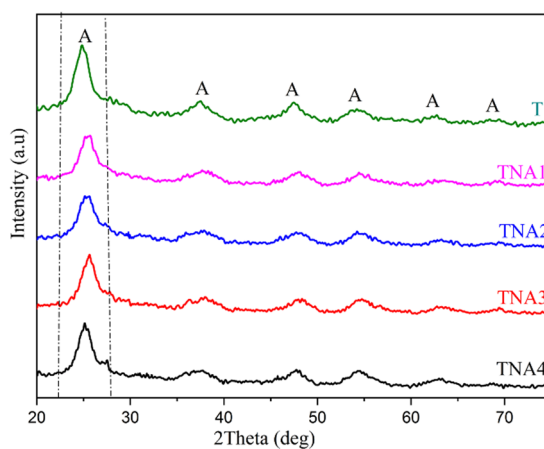
range of 260–600 °C due to structural water removal and conversion of titanium hydroxide to titanium dioxide.

As shown by the DTA curve, in the temperature range of 125–150 °C, an exothermic peak with high intensity is observed, which is related to the combustion and removal of an organic compounds from the precursor materials. The broad exothermic peak is observed at a temperature range of 200 to 500 with less intensity, which may reflect the combustion of residual organic matter (auto-ignition temp. of EAcAc = 295 °C), also, the crystallization of the anatase and rutile phases in the particles, and the phase transformation of the anatase to the rutile phase [17]. According to the DTA analysis results, temperatures of 350, 450, 550, and 650 °C were selected as the sample calcination temperature.

3.2 Phase analysis and absorption spectra of samples at 350 °C

Figure 3 shows the results of X-ray diffraction of pure and Nb/Ag-codoped TiO$_2$ samples synthesis by the sol–gel method that calcined at 350 °C for 1 h. The X-ray diffraction patterns of all samples at angles 25.45, 37.5, 47.7, 54.3, and 62.9 corresponding's to the crystalline phase of anatase with miller index (101), (004), (200), (105), and (204). The XRD pattern of all samples corresponds to the JCPDS card no.: 21–1272. The peaks of the synthesized titania sample in the presence of Ag/Nb dopants are similar to pure sample peaks. In the doped samples, the crystal peaks shift to lower angles that can be attributed to the ionic radius of Ag$^+$ (1.290 Å) and Nb^{5+} (0.64 Å), which is larger than Ti^{4+} (0.605 Å)) [18, 19]. In Fig. 3, no traces of AgO and Nb$_2$O$_5$ metal oxide peaks as well as Nb^{5+} and Ag^{2+} cations were observed in any of the samples, indicating the substitution of metal cations in the titania lattice.

Table 2 Characteristic of pure (T) and doped TiO$_2$ (TNA) mesoporous nanoparticles calcined at 350 °C (calcination time = 1 h). (d: crystallite size (nm), %A: amount of anatase phase, %R: amount of rutile phase, d_A: anatase crystallite size, d_R: rutile crystallite size, BET: specific surface area)

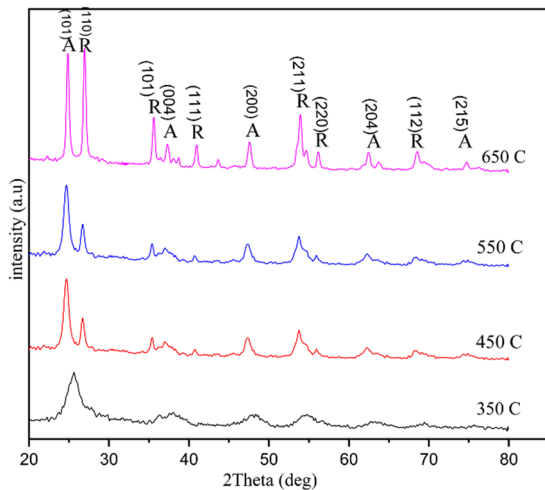| Sample	%Ag	%Nb	%A	$d_{(hkl)}$ (A^0)	β (rad)	d_A (nm)	$a = b$ (A^0)	c (A^0)	$V_{u.c}$ (A^3)	BET (m^2/g)
T	–	–	100	3.59	0.19	7.7	3.69	9.32	126.9	422.53
TNA1	0.1	0.1	100	3.5	0.59	3.7	3.78	9.23	131.74	431.34
TNA2	0.5	0.25	100	3.5	0.71	3.55	3.78	9.61	135.2	439.23
TNA3	1	0.5	100	3.5	0.47	3.1	3.79	9.32	131.45	502.72
TNA4	1	0.1	100	3.55	0.41	3.64	3.81	13.56	195.8	428.26

Fig. 4 XRD patterns of the TNA3 mesoporous nanoparticles calcined at different temperatures for 1 h (A: anatase, R: rutile)

Table 2 shows the physical properties (crystalline phases content ($A\%$), the crystallite size (d_A), lattice parameter (a, b, c), and specific surface area (BET)) of calcined TiO$_2$ sample at 350 °C. Changes in the lattice parameter and unit cell volume are due to the presence of dopant (Nb/Ag). This has caused the peaks to shift to lower angles. Also, in the presence of dopants, the size of the crystals decreased and the unit cell volume increased. The specific surface area of the doped titania (TNA) is increased compared to the pure titania (T), which can be attributed to the decrease in crystallite size in the presence of dopant [20].

3.3 Phase analysis and optical properties of TNA3 sample at different temperatures

Figure 4 shows the XRD results of TNA3 mesoporous nanoparticles calcined at 350, 450, 550, and 650 °C for 1 h in the air atmosphere. Increased calcination temperature is associated with two phenomena: (a) particle size growth, and (b) phase transformation from anatase to rutile. As the temperature increases, the phase transformation of anatase to rutile occurs.

The XRD pattern of the synthesized sample (TNA3) at 350 °C has a 100% anatase phase (Table 3). The peaks are wide and lower intensity. The reason for this phenomenon is that the particle crystallization process is not complete at this temperature [21]. At the calcination temperatures of 450, 550, and 650 °C, a mixture of two phases, anatase, and rutile, is crystallized. As the temperature rises to 450 °C, the phase transformation of anatase to rutile occurs, which includes 69% of the anatase phase and 31% of the rutile phase. The crystallization of the particles and the intensity of the peaks at this temperature are more than 350 °C. The X-ray diffraction pattern of the specimens (Temp. 450, 550, 650 °C) at angles 25.3, 37.6, 47.9, 62.8, and 74.9 related to the crystalline phase of anatase, respectively, with the miller index (101), (004), (200), (204), and (215) with JCPDS code 21–1272 and angles of 34.37, 35.8, 41.4, 54.23, 56.4, and 69.5 related to the crystal phase of rutile, respectively, it is consistent with the miller index (110), (101), (111), (211), (220), and (221) with the reference JCPDS code 12–1276. Also, with increasing temperature up to 550 °C, the percentage of anatase phase (61%) and rutile phase (39%) compared to the 450 °C sample decreased and increased, respectively, indicating particle growth. When the temperature rises to 650 °C, the phase transformation of anatase to rutile increases, and the percentage of anatase phase decreases, and the rutile increases (Table 3). Adding dopant increases the surface defect of the nanoparticles and transfers the anatase phase transformation temperature to the rutile at lower temperatures. Also, the concentration of oxygen vacuum increases at the surface of anatase grains [22, 23].

The diffraction peaks of crystal planes (101), (200), and (204) of anatase phase in XRD patterns were selected to determine the lattice parameters (Table 3) of the TiO$_2$ and doped TiO$_2$ nanopowders. The lattice parameters were obtained by using the Eq. 4 [16]

$$\begin{aligned} &(\text{Bragg's law}) : 2d_{(hkl)} \sin \theta = \lambda \\ &\left(1/d_{(hkl)}\right)^2 = (h/a)^2 + (k/b)^2 + (l/c)^2 \end{aligned} \tag{4}$$

where $d_{(hkl)}$ is the lattice distance between the crystal planes of (h k l); λ is the wavelength of X-ray used in the

Table 3 The physical properties of the TNA3 mesoporous nanoparticles calcined at different temperatures (calcination time = 1 h)
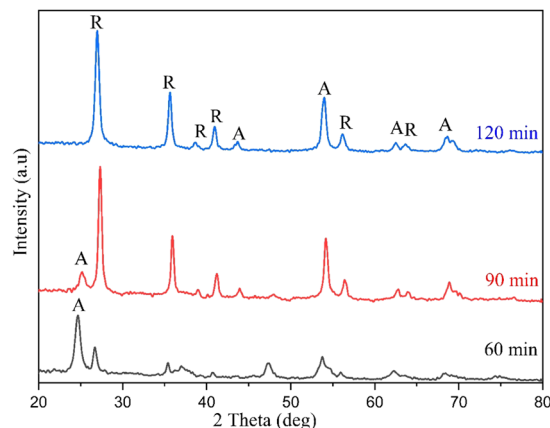
Calcination temperature	%A	%R	d_A (nm)	d_R (nm)	Anatase phase			Rutile phase			BET (m²/g)
					$a = b$ (A⁰)	c (A⁰)	$V_{u.c}$ (A³)	$a = b$ (A⁰)	c (A⁰)	$V_{u.c}$ (A³)	
350	100	–	3.1	–	3.79	9.32	131.45	–	–	–	502.27
450	69	31	5.07	9.5	3.83	10.41	153.23	3.33	2.13	23.41	118.74
550	61	39	7.49	9.5	3.71	13.45	187.76	3.35	1.42	15.49	180.92
650	33	57	11	11.94	7.58	5.71	327.51	3.43	3.39	39.18	155.07
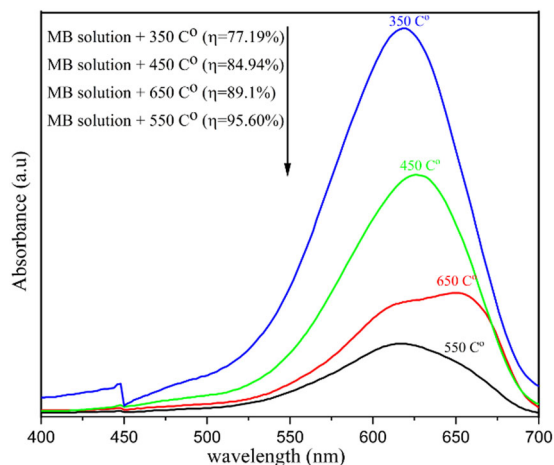
Fig. 5 The absorption spectra of MB solution under visible light for 2 h in the presence of TNA3 calcined at different temperatures

Fig. 6 XRD pattern of TNA3 calcined at 550 °C for different calcination times

experiment; θ is the diffraction angle of the crystal plane (h k l); h k l is the crystal plane index; and a, b, and c are lattice parameters (in anatase form, $a = b \neq c$).

As the temperature rises to 650 °C (Table 3), the crystallite size of the anatase and rutile phase increases. Also, the lattice parameter and cell volume have increased (131.45 to 327.51 A³ for anatase phase) and the specific surface area has also decreased (502 to 155 m²/g), which is due to the effect of temperature on particle size growth and phase transformation of anatase to the rutile of the synthesized samples [24].

The results of the absorption spectrum of MB solution in the presence of TNA3 calcined at different temperatures are shown in Fig. 5. The highest percentage of photocatalytic degradation (Fig. 5: inset) is related to the 550 °C sample. Temperatures of 450, 550, and 650 °C include two phases of anatase and rutile (Fig. 4 and Table 3), so they have a higher photocatalytic degradation than the 350 °C sample (100% anatase) [25]. Also, the 550 °C sample has the highest percentage of photocatalytic degradation due to its higher specific surface area (180.92 m²/g) than other samples. The rutile phase is the main factor separating electrons and holes. The electrons stimulated in the rutile phase transfer themselves to the anatase phase conduction band

and form a hole in the rutile phase, thereby reducing the electron–hole recombination [26].

### 3.4 Phase analysis and optical properties of TNA3 sample at different calcination times

Figure 6 shows the XRD results of the TNA3 calcined at 550 °C for 60, 90, and 120 min. For 60 min, the calcined sample has a higher anatase phase percentage than other times.

As the calcination time increases, the type and percentage of crystalline phases formed change (Table 4). As the calcination time increases, the percentage of the rutile phase increases. Also, as time goes on, the size of the crystals increases and, the surface area of the particles decreases (180.92 to 89.72 m²/g) because the particles will take time to grow.

Figure 7 shows the absorption spectra of MB solution in the presence of the TNA3 sample calcined at 550 °C for 60, 90, and 120 min. The highest content of photocatalytic degradation occurs within 60 min (inset). With increasing calcination time, crystalline growth and, increasing the content of the rutile phase in the samples (Table 4), these two factors lead to a decrease in the content of photocatalytic degradation.
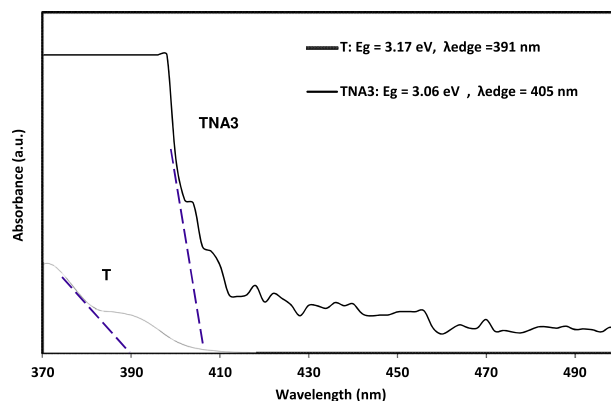
Table 4 The physical properties of the TNA3 mesoporous nanoparticles calcined at different calcination times (calcination temperature = 550 °C)

Calcination time (min)	%A	%R	d_A (nm)	d_R (nm)	Anatase phase			Rutile phase			BET (m^2/g)
					$a = b$ (A^0)	c (A^0)	$V_{u.c}$ (A^3)	$a = b$ (A^0)	c (A^0)	$V_{u.c}$ (A^3)	
60	61	39	7.49	9.5	3.71	13.45	187.76	3.35	1.42	15.49	180.92
90	15	85	5.92	10.66	3.78	12.72	180.98	3.27	4.49	48.01	143.24
120	9	91	4.08	10.91	6.49	5.73	241.32	3.29	6.25	67.65	89.72
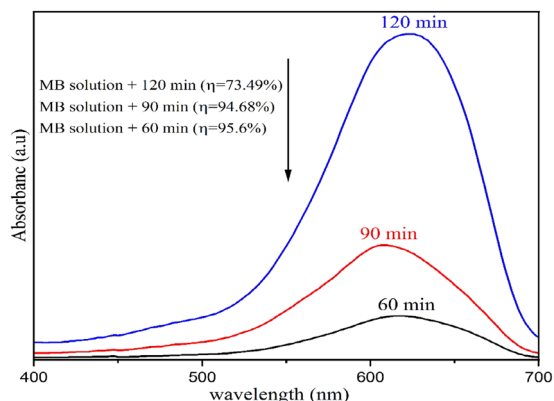
Fig. 7 The absorption spectra of MB solution under visible light in the presence of TNA3 sample calcined at 550 °C for different calcination times

Fig. 8 UV–Vis spectra of T and TNA3 samples calcined at 550 °C for 1 h

## 3.5 Optical band gap of T and TNA3 at 550 °C calcination temperature

The results of the band gap energy (E_g) for pure titania (T) and TNA3 calcined at 550 °C are shown in Fig. 8. The addition of metal dopant to T sample can reduce the band gap energy. The dopant can create an electron-saturated surface in the titania band gap that easily stimulates the conduction band (CB), or by creating a hole filled surface at the titania valance band (VB), stimulates the valance band of titania [27], so the creation of a new electron junction surface in the titania band gap leads to a reduction in the band gap energy (Fig. 8, inset: E_g and λ_{edge}). With the addition of Nb and Ag dopant, the absorption intensity in the visible light area increases, and the absorption edge shifted (Redshift) to the visible light wavelength (Fig. 8, inset) [28]. Doping of Nb and Ag cations in the TiO$_2$ structure has led to an increase in oxygen vacancy, which is one of the effective factors in the photocatalytic process [29]. The oxygen vacancies are active groups, which can easily combine with other atoms or groups and become stable. It accounts for an increase in the amount of surface hydroxyl oxygen. Increase in surface hydroxyl is favorable for photocatalytic reactions. The hydroxyl content (O_L and

O_H%) is the ratio of the area of corresponding peak to the total area of the two O 1 s peaks. According to XPS result, O_L and O_H percent for T and TNA3 samples are as below:

T sample: O_L: 63.4%, O_H: 36.6% and TNA3 sample: O_L: 49.7%, O_H: 50.3%.

3.6 The effect of visible light irradiation time on photocatalytic efficiency

Figure 9 shows the photocatalytic degradation efficiency of MB solution in the presence of calcined T and TNA3 samples at 550 °C at different times of visible light radiation. The photocatalytic efficiency for T, TNA3 samples after 2 h of visible light radiation is 63.25% and 95.60% (Fig. 10, inset), respectively. According to Fig. 10, we see that the percentage of degradation of MB solution in the first hour is higher than in the second hour. In other words, the rate of reaction of the dye solution is reduced by increasing the irradiation time. This result indicates that active photocatalytic sites are deactivated by powder coagulation and reduce the longevity of photocatalytic activity. One of the important factors on the photocatalytic degradation efficiency of the MB solution is the specific surface area (BET) of the nanoparticles [30–32]. By comparing the T and TNA3 sample (Fig. 10a, b), the specific surface area (BET) are equal to 143.23 and
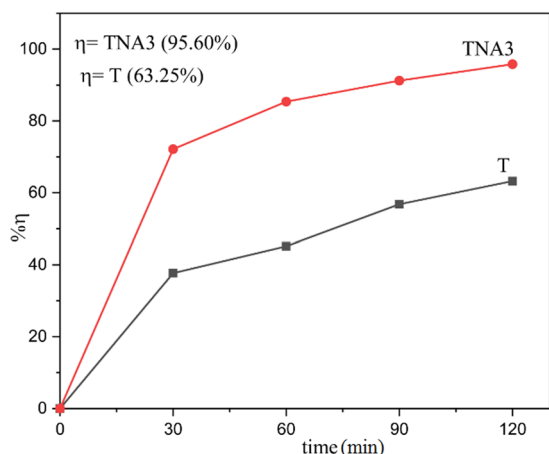
Fig. 9 Photocatalytic degradation of the MB solution in the presence of T and TNA3 samples calcined at 550 °C under 2 h visible light irradiation
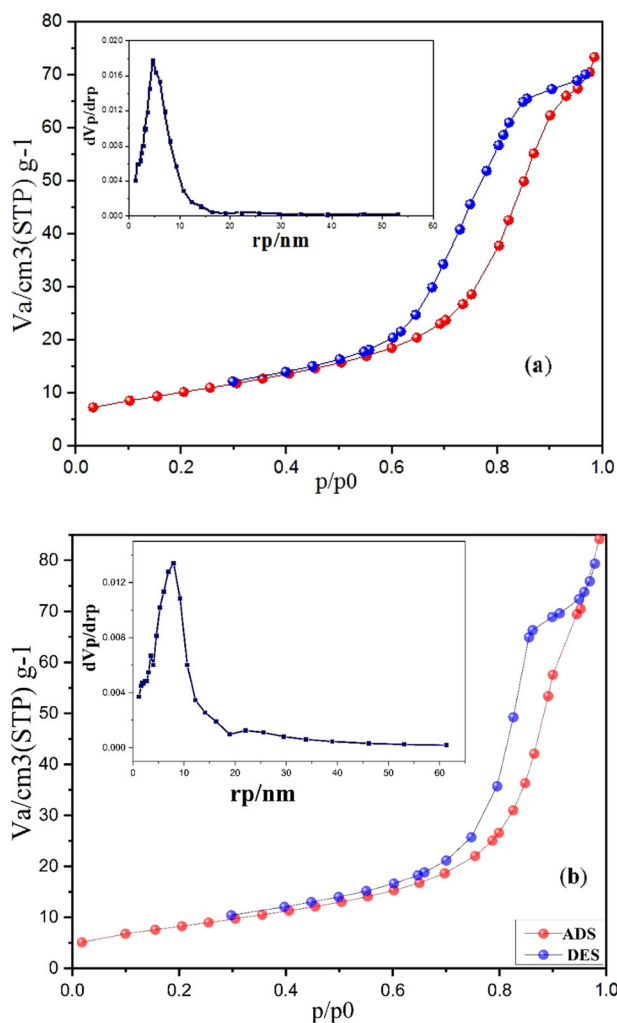
Fig. 10 N$_2$ physisorption isotherms (BET) and pore size distribution (BJH = inset) of **a** TiO$_2$ (sample code: T) and **b** Nb/Ag-codoped TiO$_2$ mesoporous nanoparticles (sample code: TNA3) calcined at 550 °C

180.92 m^2/g, respectively. N$_2$ adsorption–desorption isotherms of the T (Fig. 10a) and TNA3 (Fig. 10b) samples calcined at 550 °C are shown in Fig. 10a, b. The pore size distribution (BJH) is shown an inset in respective isotherms. The adsorption–desorption isotherms of both samples are based on IUPAC classification compatible with type IV, and the hysteresis loop is H2 and H1, respectively [33, 34]. The hysteresis loop for both samples is mesoporous. The pores in the pure sample (H2) have a narrow-span shape with uniform channels connected in the lattice. The structure of these pores is mesoporous. For TNA3, the particles are spherical and cylindrical, and the hysteresis loop represents the porous material [35]. For T sample, the mean pore diameter is about 17.06 nm and the pore size distribution (BJH) is in the range of 1.2–61.3 nm (Fig. 10a, inset) and for TNA3, the average pore diameter is about 12.31 nm and the pore size distribution is in the range of 1.2–53 nm (Fig. 10b, inset). As can be seen, the TNA3 sample has a higher specific surface area relative to the pure sample, which is one of the effective factors in improving photocatalytic properties and increasing photocatalytic efficiency.

## 3.7 XPS analysis of T and TNA3 samples calcined at 550 °C

XPS analysis was performed as a result of a more detailed study of the effect of Ag and Nb dopants on the phase transformation of anatase to rutile, formation of oxygen vacancy, and identification of Ti, Nb, and Ag elements with the desired valence number. Figure 11 shows the XPS analysis for pure TiO$_2$ nanoparticles (T, Fig. 11a) and TNA3 (Fig. 11b) samples.

By replacing ions with a charge of <4, such as Ag$^+$, in the TiO$_2$ crystal lattice, the oxygen vacancy increases and, eventually the phase transformation rate of anatase to rutile increases [36, 37]. On the other hand, replacing the ion with a charge of >4, such as Nb^{+5} in the TiO$_2$ crystal lattice, has led to a reduction in the oxygen vacancy, which prevents the phase transformation of anatase to rutile [38].

Figure 11a, b clearly shows the elements Ti, C, and O. Weak peaks of Ag and Nb are shown in Fig. 11b of the XPS spectra. The C 1s peak is attributed to adventitious hydrocarbon contamination from the instrument [39]. Comparing Ti 2p$_{3/2}$ and Ti 2p$_{1/2}$ with pure and doped samples (TNA3), we see that there has been a change in the Ti oxidation state, which can be divided into Ti 2p1 and Ti 2p3 electronic rotation circuit attributed.

According to Fig. 11a, b, the binding energy of 459.2 eV corresponds to Ti 2p$_{1/2}$ and the binding energy of 464.7 eV corresponds to Ti 2p$_{3/2}$ (Fig. 11a) in accordance with the Ti^{4+} oxidation state [40], while the peaks located at 458.8 and 464.1 eV belong to Ti 2p$_{3/2}$ and Ti 2p$_{1/2}$ of the Ti^{3+} (Fig. 11c), respectively [41]. The binding
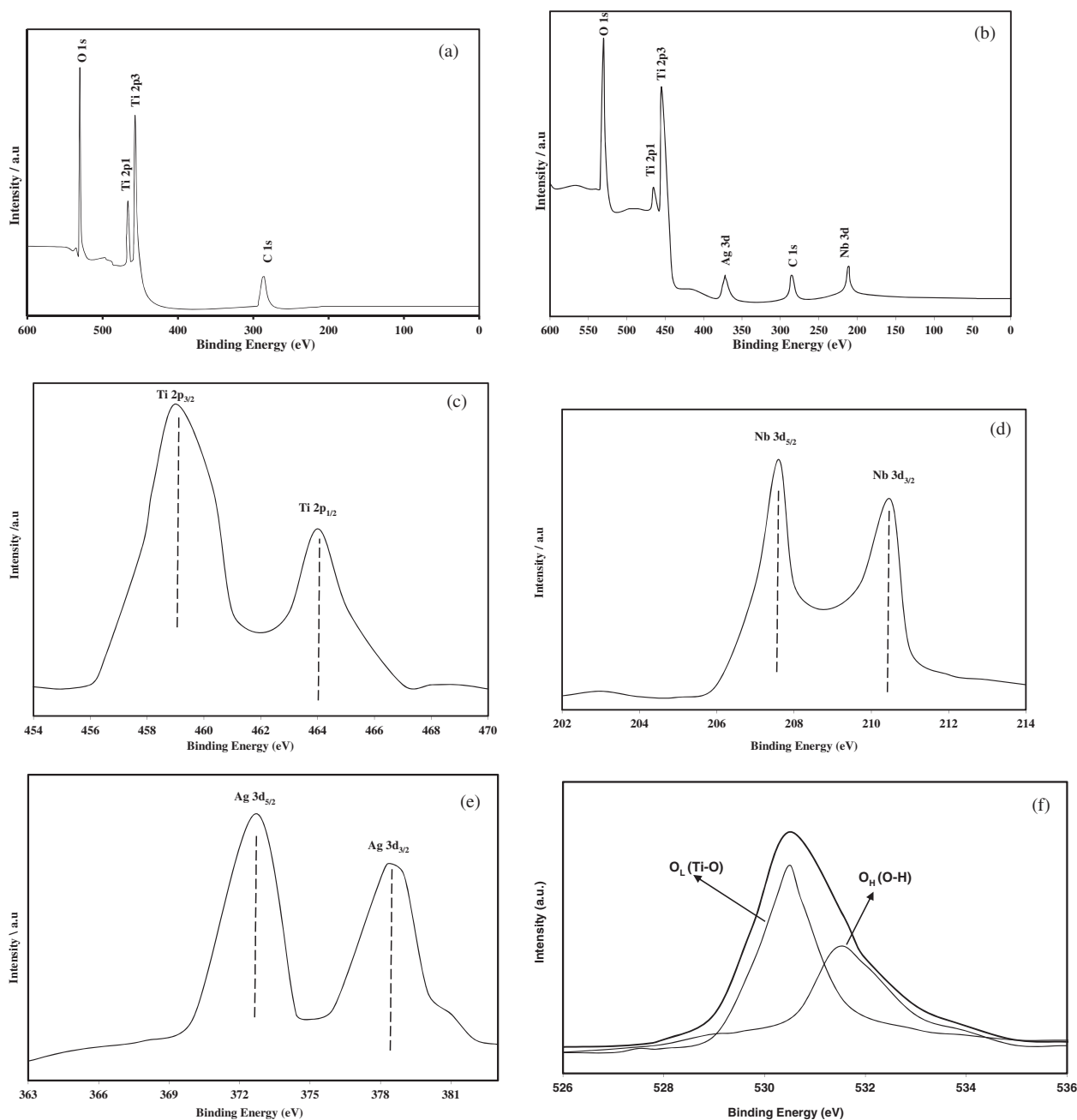
Fig. 11 **a** XPS survey spectra of TiO_2 pure (T) sample, **b** survey spectra of TNA3, high-resolution XPS spectra of **c** Ti 2p, **d** Nb 3d, **e** Ag 3d, and **f** O1s for TNA3 sample

energies of Ti $2p_{3/2}$ and Ti $2p_{1/2}$ shifted to higher values after the addition of Nb^{5+} compared to pure TiO_2. This shift can prove the existence of Ti with lower valence.

Figure 11d shows two peaks of Nb 3d in the range 207.1 eV ($Nb3d_{5/2}$) and 209.9 eV (Nb $3d_{3/2}$) [42]. These peaks are formed by the rotation of an electron circuit with an energy equal to 2.6 eV. The main peak for Nb $3d_{5/2}$ is in the about of 211 eV, which corresponds to the oxidation state of Nb^{5+}.

Figure 11e shows the Ag3d spectrum of the TNA3 sample. The two peaks specified in 366.8 and 373.1 are related to $Ag3d_{5/2}$ and $Ag3d_{3/2}$. There is a difference in energy of the 6.3 eV between the binding energy of $Ag3d_{5/2}$ and $Ag3d_{3/2}$ peaks, indicating that the Ag is Ag^0 state on the TiO_2 lattice [43]. The Ti 2p peaks of TNA3 shift to lower band energy by 0.4 eV as compared to those of the T sample. This may be because since during the photo-deposition of Ag metal, some electrons migrate from Ag to Ti^{4+} and cause it to form Ti^{3+}.
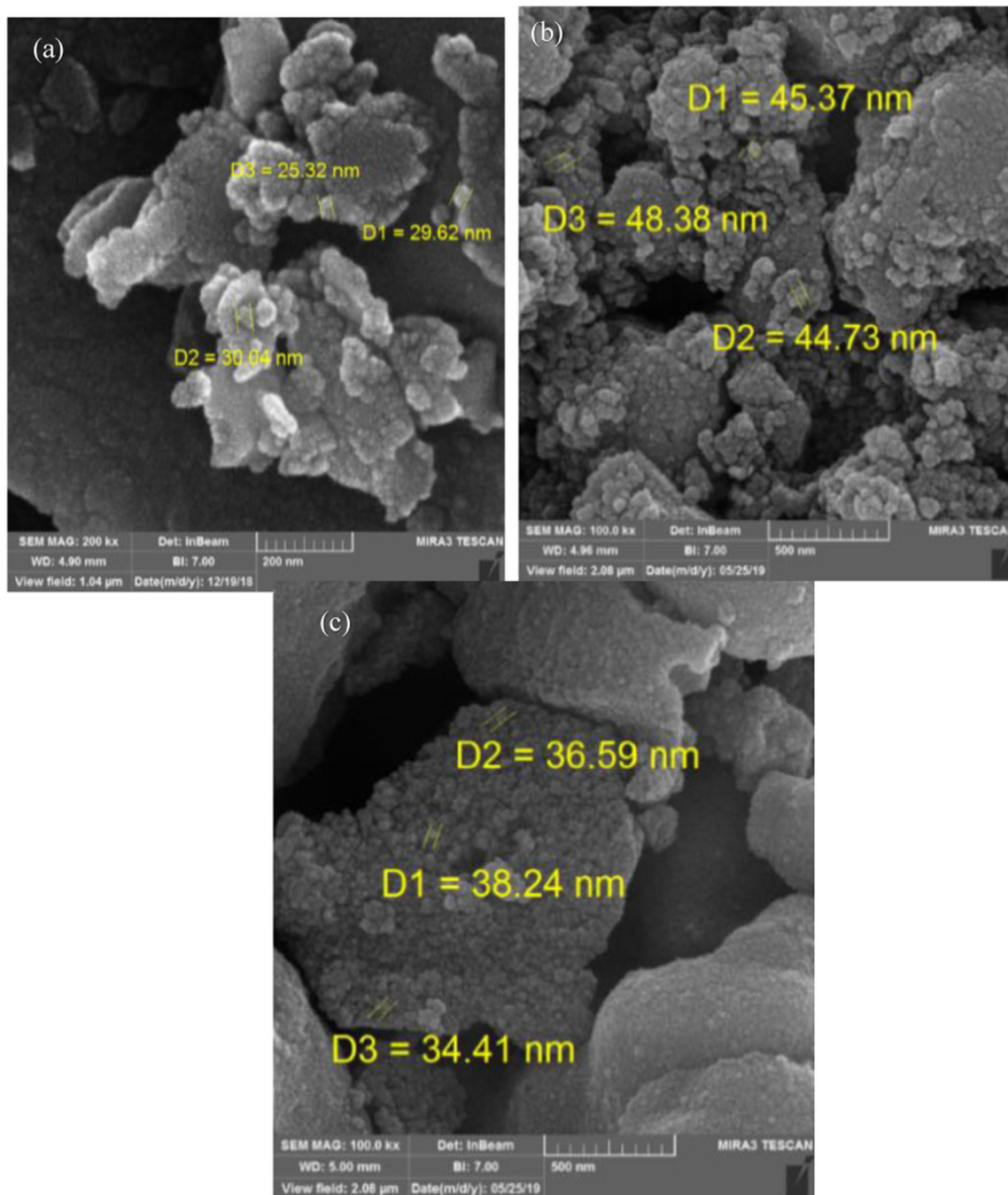
**Fig. 12** FESEM of nanoparticles. **a** Pure TiO$_2$ nanoparticle (T) calcined at 350 °C, **b** Pure TiO$_2$ nanoparticle (T) calcined at 550 °C, **c** TNA3 nanoparticle (T) calcined at 550 °C

Figure 11f, O 1s show that the peak in the about of 528.75 eV represents the metal oxides that O 1s is the lattice oxygen (O_L: Ti–O) of titania (Ti^{4+}). The peak at 530.6 eV belongs to the surface related hydroxyl group (O_H: O–H). The peaks of T2p, O1s in the XPS spectrum of the TNA3 compound indicate the presence of oxygen vacancies, which is useful for the photocatalytic process because it leads to the separation of the electron–hole pair [44].

3.8 FESEM, EDS, and maps analysis of T and TNA3 samples

Figure 12 show FESEM images of pure TiO$_2$ (T) sample calcined at 350, 550 °C (Fig. 12a, b), and TNA3 sample calcined at 550 °C (Fig. 12c). Electron microscopy images of pure TiO$_2$ specimens (Fig. 12a) have irregular nanoparticle shape and uniform particle size, while for samples in

Fig. 13 Energy dispersive X-ray spectroscopy (EDX) of T and TNA3 calcined at 550 °C
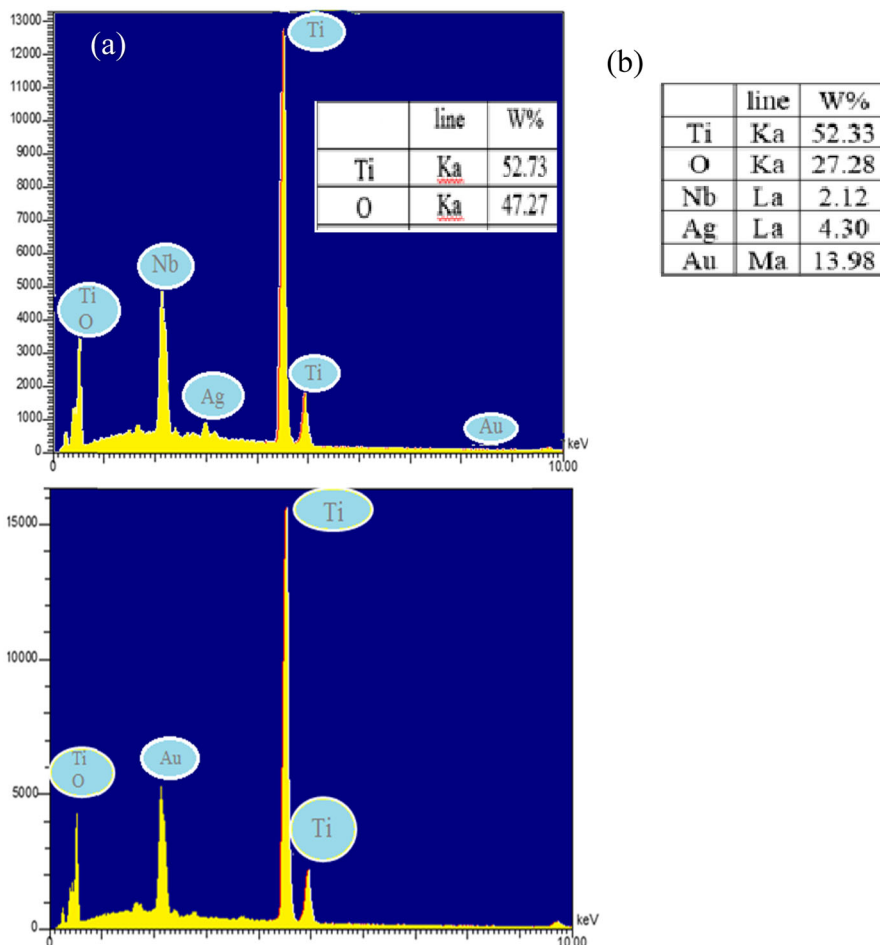
the presence of dopant (Fig. 12c, TNA3), regular nanoparticle shape and uniform particle size. The average particle size of pure TiO_2 (T) calcined at 350 and 550 °C is about 29, 46 nm, respectively, indicating particle growth. The particle size of the TNA3 sample decreased in comparison to the pure (T) sample. The average particle size of the calcined TNA3 sample at 550 °C is smaller than that of the pure sample due to the presence of dopant. The average particle size of the TNA3 sample calcined at 550 °C is about 36 nm.

The presence and distribution of elements in the pure TiO_2 sample (Fig. 13a) and TNA3 (Fig. 13b) samples calcined at 550 °C were analyzed by energy dispersive X-ray spectroscopy (EDS). The EDS analysis confirmed the presence of titanium, oxygen, niobium and silver in the synthesized TNA3 sample. The EDS spectrum of TNA3 contained high-intensity peaks of titanium, niobium, and silver.

As shown in Fig. 14, the elemental mapping of O and Ti in a sample of T (Fig. 14a) and Nb, Ag, Ti, and O in sample TNA3 (Fig. 14b) demonstrate that all four elements are distributed throughout the TNA3 nanostructures. According to MAP images, the elements of the synthesized samples

can be seen that the oxygen distribution in T nanoparticles (Fig. 14a) is higher than the TNA3 sample. Also, according to the EDX results (Fig. 13a, b), it was observed that the oxygen content in the pure sample was 47.27% more than oxygen content in the TNA3 sample (27.28%). As mentioned earlier, the effect of dopant (Nb and Ag) by reducing the oxygen vacancy has reduced the amount of oxygen in the TNA3 sample.

4 Conclusion

In this research, Nb and Ag-codoped TiO_2 mesoporous nanoparticles with photocatalytic activities have been synthesized via sol–gel method. The effects of metal ion doping and calcination temperature (350–650 °C) on the crystallization of anatase and rutile phase, crystallite size, and optical properties of TiO_2 mesoporous nanoparticles has been investigated.

The averages particle sizes of the prepared samples varied from 29 to 46 nm with an increase in calcination temperature. The size of the crystallites in doped TiO_2 samples is smaller

Fig. 14 Elemental mapping images for the **a** Pure TiO_2 (T) and **b** TNA3 samples calcined at 550 °C
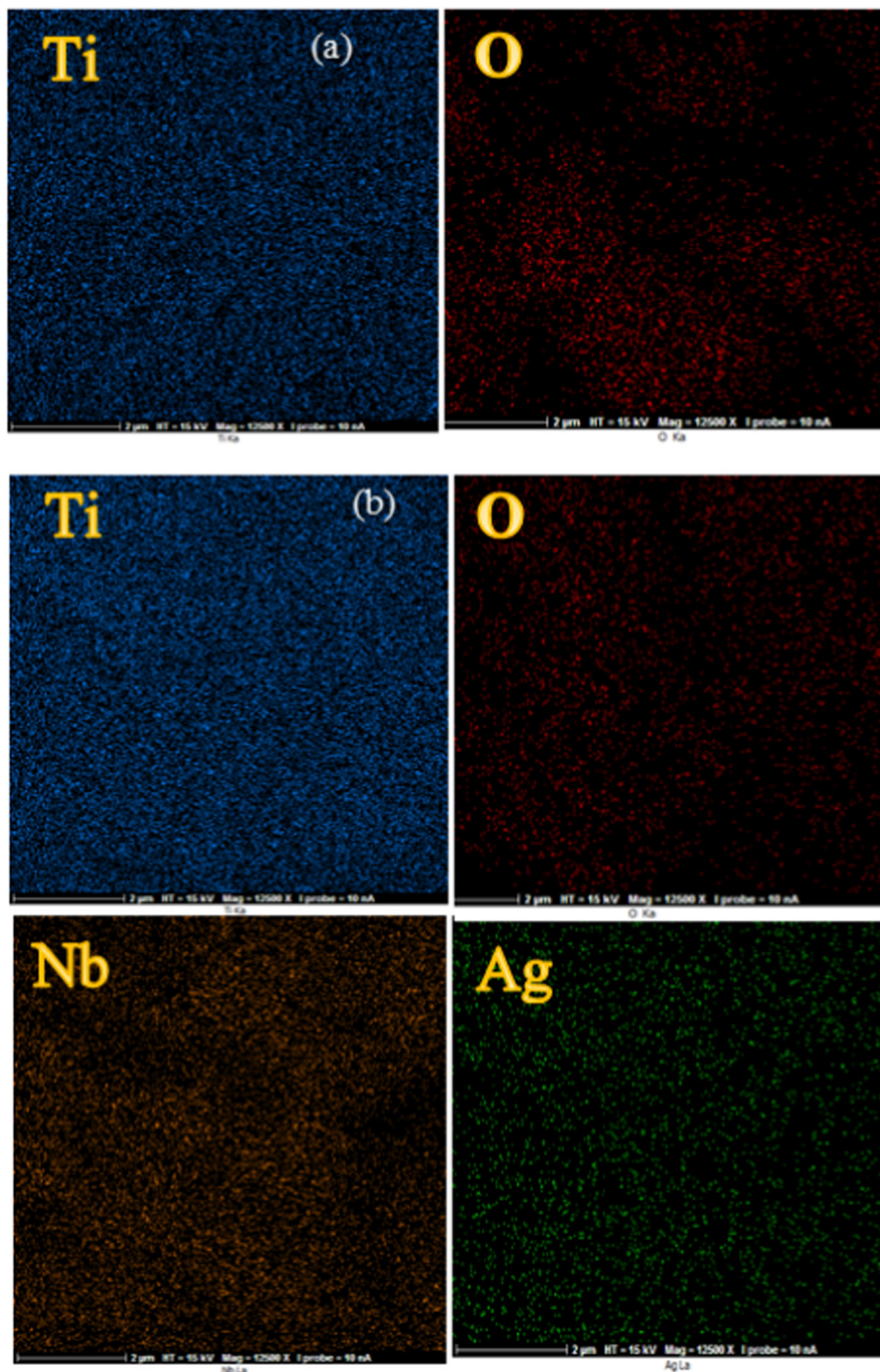
than those in the undoped sample, suggesting that dopants have an inhibiting role on the grain growth. The photocatalytic activity of the doped nanopowders is higher than that of pure TiO_2 nanoparticles. Nb^{+5} and Ag^+ substitution for Ti^{4+} in the titania lattice results in a decrease in the rate of photogenerated electron–hole recombination that is responsible for the enhancement in photocatalytic degradation rate. It is found that the Nb, Ag-codoped TiO_2 exhibited the highest photocatalytic activity under visible light irradiation compared with undoped TiO_2 because the co-operation of Ag and Nb not only led to the much narrowing of the band gap, but also promoted the separation of the photogenerated electrons and holes.

Compliance with ethical standards

References

1. Ramrez RJ, Arellano CAP, Varia JC, Martinez SS (2015) Visible light-induced photocatalytic elimination of organic pollutants by TiO2: a review. Curr Org Chem 19:540–555
2. Wang W, Wang S, Lv J, Zhao M, Zhang M, He G, Fang C, Li L, Sun Z (2018) Enhanced photoresponse and photocatalytic activities of graphene quantum dots sensitized Ag/TiO2 thin film. J Am Ceram Soc 101:5469–5476
3. Wang Z, Liu S, Cao X, Wu S, Liu CQ, Li G, Jiang W, Wang H, Wang N, Ding W (2020) Preparation and characterization of TiO2 nanoparticles by two different precipitation Methods. Ceram Int 46:15333–15341
4. Krol RV, Liang Y, Schoonman J (2008) Solar hydrogen production with nanostructured metal oxides. J Mater Chem 18:2311–2320
5. Parida KM, Sahu N (2008) Visible light induced photocatalytic activity of rare earth titania nanocomposites. J Mol Catal A: Chem 287:151–158
6. Khan MM, Ansari SA, Lee J, Cho MH (2013) Highly visible light active Ag@TiO2 nanocomposites synthesized using an electrochemically active biofilm: a novel biogenic approach. Nanoscale 5:4427–4435
7. Chen Z, Fang L, Dong W, Zheng F, Shen M, Wang J (2014) Inverse opal structured Ag/TiO2 plasmonic photocatalyst prepared by pulsed current deposition and its enhanced visible light photocatalytic activity. J Mater Chem A 2:824–832
8. Kalathil S, Khan MM, Ansari SA, Lee J, Cho MH (2013) Band gap narrowing of titanium dioxide (TiO2) nanocrystals by electrochemically active biofilms and their visible light activity. Nanoscale 5:6323–6326
9. Assayehegn E, Solaiappan A, Chebude Y, Alemayehu E (2020) Fabrication of tunable anatase/rutile heterojunction N/TiO2 nanophotocatalyst for enhanced visible light degradation activity. Appl Sur Sci 515:145966
10. Chen X, Liu L, Huang F (2015) Black titanium dioxide (TiO2) nanomaterials. Chem Soc Rev 44:1861–1885
11. Liu X, Gao S, Xu H, Lou Z, Wang W, Huang B, Dai Y (2013) Green synthetic approach for Ti3+ self-doped TiO(2-x) nanoparticles with efficient visible light photocatalytic activity. Nanoscale 5:1870–1875
12. Behnajady MA, Eskandarloo H (2013) Characterization and photocatalytic activity of Ag–Cu/TiO2 nanoparticles prepared by sol–gel method. J Nanosci Nanotech 13:548–553
13. Khatun N, Tiwari S, Amin R, Tseng CM, Biring S, Sen S (2020) Stable anatase phase with a band gap in visible light region by a charge compensated Ga–V (1:1) co-doping in TiO2. Ceram Int 46:8958–8970
14. Chena Q, Zhang Y, Zhang D, Yang Y (2017) Ag and N co-doped TiO2 nanostructured photocatalyst for printingand dyeing wastewater. J Water Process Eng 16:14–20
15. Baker RW (2004) Membrane technology and application. Wiley Pub, Chichester
16. Klug P, Alexander LE (1974) X-Ray diffraction procedures. Wiley, New York
17. Zhu X, Han S, Feng W, Kong Q, Dong Z, Wang C, Lei J, Yi Q (2018) The effect of heat treatment on the anatase–rutile phase transformation and photocatalytic activity of Sn-doped TiO2 nanomaterials. Roy Soc Chem Adv 8:14249–14257
18. Khan S, Cho H, Kim D, Han SS, Lee KH, Cho SH, Song T, Choi H (2017) Defect engineering toward strong photocatalysis of Nb-doped anatase TiO2: Computational predictions and experimental verifications. Appl Catal B Envi 206:520–530
19. Suwarnkar MB, Dhabbe RS, Kadam AN, Garadkar KM (2014) Enhanced photocatalytic activity of Ag doped TiO2 nanoparticles synthesized by a microwave assisted method. Ceram Int 40:5489–5496
20. Thongyong N, Tuichai W, Chanlek N, Thongbai P (2017) Effect of Zn2+ and Nb5+ co-doping ions on giant dielectric properties of rutile-TiO2 ceramics. Ceram Int 43:15466–15471
21. Zhou M, Yu J, Liu S, Zhai P, Jiang L (2008) Effects of calcination temperatures on photocatalytic activity of SnO2/TiO2 composite films prepared by an EPD method. J Hazard Mater 154:1141–1148
22. Rath C, Mohanty P, Pandey AC, Mishra NC (2009) Oxygen vacancy induced structural phase transformation in TiO2 nanoparticles. J Phys D Appl Phys 42:205101
23. Koozegar Kaleji B, Mirzaee S, Ghahramani S, Rezaie S, Hosseinabadi N, Fujishima A (2018) Sol-gel synthesis of Sn/Fe co-doped TiO2 nanoparticles: Study of Structural, Optical and Photocatalytic properties. J Mater Sci Mater Elect 29:12351–12359
24. Mahshid S, Askari M, Ghamsari MS (2007) Synthesis of TiO2 nanoparticles by hydrolysis and peptization of titanium isopropoxide solution. J Mater Process Technol 189:296–300
25. Su R, Bechstein R, Sø L, Vang RT, Sillassen M, Esbjörnsson B, Palmqvist A, F. Besenbacher F (2011) How the anatase-to-rutile ratio influences the photoreactivity of TiO2. J Phys Chem C 115:24287–24292
26. Hurum DC, Agrios AG, Gray KA, Rajh T, Thurnauer MC (2003) Explaining the enhanced photocatalytic activity of degussa P25 mixed-phase TiO2 using EPR. J Phys Chem B 107:4545–4549
27. Kočí K, Obalová L, Lacný Z (2008) Photocatalytic reduction of CO2 over TiO2 based catalysts. Chem Pap 62:1–9
28. Su H, Huang YT, Chang YH, Zhai P, Hau NY, Cheung PCH, Yeh WT, Wei TC, Feng SP (2015) The synthesis of Nb-doped TiO2 nanoparticles for improved-performance dye sensitized solar cells. Electrochim Acta 182:230–237
29. Kim SG, Ju MJ, Choi IT, Choi WS, Choi HJ, Baek JB, Kim HK (2013) Nb-doped TiO2 nanoparticles for organic dye-sensitized solar cells. RSC Adv 3:16380–16386
30. Koozegar Kaleji B, Gorgani M, Comparison of sol-gel and hydrothermal synthesis methods on the structural, optical and photocatalytic properties of Nb/Ag codoped TiO2 mesoporous nanoparticles (2020). https://doi.org/10.1080/03067319.2020.1767096

31. He HY, Lu J (2017) Highly photocatalytic activities of magnetically separable reduced graphene oxide-CoFe$_2$O$_4$ hybrid nanostructures in dye photodegradation. Sep Purif Technol 172:374–381

32. He HY, He Z, Shen Q (2018) Efficient hydrogen evolution catalytic activity of graphene/metallic MoS$_2$ nanosheet heterostructures synthesized by a one-step hydrothermal process. Int J Hydrog Energy 43(48):21835–21843

33. Yu JC, Zhang L, Zheng Z, Zhao J (2003) Synthesis and characterization of phosphated mesoporous titanium dioxide with high photocatalytic activity. Chem Mater 15:2280–2286

34. Wark M, Tschirch J, Bartels O, Bahnemann D, Rathouský J (2005) Photocatalytic activity of hydrophobized mesoporous thin films of TiO$_2$. Microporous Mesoporous Mater 84:247–253

35. Rouquerol J, Rouquerol F, Llewellyn P, Maurin G, Sing K (2014) Adsorption by powders and porous solids principles, methodology and applications, 2nd edn., Elsevier, France

36. Arroyo R, Córdoba G, Padilla J, Lara V (2002) Influence of manganese ions on the anatase–rutile phase transition of TiO$_2$ prepared by the sol–gel process. Mater Lett 54:397–402

37. Wang H, Zhang N, Cheng G, Guo H, Shen Z, Yang L, Zhao Y, Alsaedi A, Hayat T, Wang X (2020) Preparing a photocatalytic Fe doped TiO$_2$/rGO for enhanced bisphenol A and its analogues degradation in water sample. Appl Sur Sci 505:144640

38. Karvinen S (2003) The effects of trace elements on the crystal properties of TiO$_2$. Solid State Sci 5:811–819

39. Duan YY, Zhang M, Wang L, Wang F, Yang LP, Li XY, Wang CY (2017) PlasmonicAg-TiO$_{2-x}$ nanocomposites for the photocatalytic removal of NO under visible light with high selectivity: the role of oxygen vacancies. Appl Catal B Environ 204:67–77

40. Shin SS, Kim JS, Suk JH, Lee KD, Kim DW, Park JH, Cho IS, Hong KS, Kim JY (2013) Improved quantum efficiency of highly efficient perovskite BaSnO$_3$-based dye-sensitized solar cells. ACS Nano 7:1027–1035

41. Jiang JJ, Xing ZP, Li M, Li ZZ, Yin JW, Kuang JY, Zou JL, Zhu Q, Zhou W (2018) Plasmon Ag decorated 3D urchinlike N-TiO$_{2-x}$ for enhanced visible-light-driven photocatalytic performance. J Colloid Interface Sci 521:102–110

42. Yang J, Zhang X, Wang C, Sun P, Wang L, Xia B, Liu Y (2012) Solar photocatalytic activities of porous Nb-doped TiO$_2$ microspheres prepared by ultrasonic spray pyrolysis. Solid State Sci 14:139–144

43. Li M, Xing ZP, Jiang JJ, Li ZZ, Yin JW, Kuang JY, Tan SY, Zhu Q, Zhou W (2018) Surface plasmon resonance-enhanced visible-light-driven photocatalysis by Ag nanoparticles decorated S-TiO$_{2-x}$ nanorods. J Taiwan Inst Chem Eng 82:198–204

44. Lu L, Wang G, Xiong Z, Hu Z, Liao Y, Wang J, Li J (2020) Enhanced photocatalytic activity under visible light by the synergistic effects of plasmonics and Ti^{3+}-doping at the Ag/TiO$_{2-x}$ heterojunction. Ceram Int 46:10667–10677